J. Fluid Mech. (2010), *vol.* 659, *pp.* 365–374.
doi:10.1017/S0022112010003216

Crossflow past a prolate spheroid at Reynolds number of 10 000

GEORGE K. EL KHOURY[1]†, HELGE I. ANDERSSON[2] AND BJØRNAR PETTERSEN[1]

[1]Department of Marine Technology, The Norwegian University of Science and Technology, NO-7491 Trondheim, Norway

[2]Department of Energy and Process Engineering, The Norwegian University of Science and Technology, NO-7491 Trondheim, Norway

(Received 30 March 2010; revised 7 June 2010; accepted 9 June 2010; first published online 2 August 2010)

The flow field around a 6:1 prolate spheroid has been investigated by means of direct numerical simulations. Contrary to earlier studies the major axis of the spheroid was oriented perpendicular to the oncoming flow. At the subcritical Reynolds number 10 000 the laminar boundary layer separated from the frontal side of the spheroid and formed an elliptical vortex sheet. The detached shear layer was unstable from its very inception and even the near-wake turned out to be turbulent. The Strouhal number associated with the large-scale shedding was 0.156, significantly below that of the wake of a sphere. A higher-frequency mode was associated with Kelvin–Helmholtz instabilities in the detached shear layer. The shape of the near-wake mirrored the shape of the spheroid. Some 10 minor diameters downstream, the major axis of the wake became aligned with the minor axis of the spheroid.

Key words: bluff body, DNS, ellipsoid, turbulent flows, wakes

1. Introduction

Flows around bluff bodies comprise a variety of complex flow phenomena which depend on the shape and orientation of the body with respect to the flow direction as well as on the Reynolds number (Re) of the flow. The wake of a circular cylinder is the prototype of two-dimensional bluff-body wakes (see e.g. Zdravkovich 1997). Similarly, the flow past a sphere is the axisymmetric prototype of bluff-body wakes. A comprehensive experimental and computational investigation of the near-wake of spheres up to $Re = 300$ by Johnson & Patel (1999) revealed how the originally steady and axisymmetric wake first became non-axisymmetric and thereafter unsteady. Large-eddy simulations of the sphere wake at Reynolds number of 10 000 by Constantinescu & Squires (2003) and Yun, Kim & Choi (2006) showed the presence of a high-frequency mode in addition to the low-frequency large-scale shedding, as already observed in a wind-tunnel study by Sakamoto & Haniu (1990). According to Yun *et al.* (2006), the vortex shedding at a Strouhal number $St \approx 0.19$ was accompanied by a broad frequency range associated with shear-layer instabilities. Constantinescu & Squires (2004) even considered the wake flow in the supercritical regime at $Re = 1.14 \times 10^6$ by means of detached-eddy simulations. However, for

† Email address for correspondence: george@ntnu.no

the subcritical flow at $Re = 10\,000$, they reported large-scale shedding at a Strouhal number 0.195 together with secondary peaks in the range $1.9 \leqslant St \leqslant 2.4$.

A prolate spheroid is a three-dimensional body with two different length scales, one plane of symmetry and one axis of symmetry. The ratio between the semimajor and semiminor axes, i.e. the aspect ratio, is a measure of departure from a spherical body. Spheroids with aspect ratios 8:1, 6:1 and 3:1 can be considered as simplified models of submarines, unmanned underwater vehicles, missiles, airships, etc. When the aspect ratio is relatively high and the major axis is aligned with the flow the prolate spheroid behaves as a slender body. The three-dimensional flow separation and the wake flow become gradually more complex with increasing angle of attack. Han & Patel (1979), for instance, presented results of a detailed experimental investigation of a 4.3:1 spheroid whereas Wikström *et al.* (2004) performed large-eddy simulations of flow past a 6:1 spheroid at incidence. None of the comprehensive studies published on flow around prolate spheroids at incidence seem to exceed 30° angle of attack.

The aim of this study is therefore to examine the flow over a 6:1 prolate spheroid at high incidence. The major axis is taken to be perpendicular, i.e. at 90°, to the main flow direction. With this orientation the spheroid plays the role of a bluff body rather than a slender object. The Reynolds number based on the minor axis diameter is taken to be 10 000, which matches that considered in the large-eddy simulation studies of wakes behind spheres by Constantinescu & Squires (2003) and Yun *et al.* (2006). At this Reynolds number the vortex sheet separating from the surface immediately becomes turbulent (see e.g. Sakamoto & Haniu 1990).

The wake behind a prolate spheroid without incidence is axisymmetric, at least at low Re, just as is the wake of a sphere. The axisymmetry is broken by the incidence angle and in the particular case of 90° angle of attack it can be anticipated that the wake at mid-span will resemble the wake behind circular cylinders. At a substantially lower Reynolds number, Sheard, Thompson & Hourigan (2008) reported that the vortices shed in the vicinity of the cylinder mid-span resembled Kármán vortices when the length-to-diameter ratio exceeded 4. The helical-like wake which may occur behind a sphere at higher Re due to the shedding of hairpin vortices at varying azimuthal locations will probably be prohibited in a wake behind a prolate spheroid in crossflow provided that the aspect ratio is sufficiently above 1.

The frontal area of the prolate spheroid in crossflow is elliptical. At least in the far wake, one may expect that the flow would resemble the wake formed behind sharp-edged elliptical disks. Kuo & Baldwin (1967) and more recently Kiya & Abe (1999) observed a puzzling switching of the axes so that the major axis of the elliptical wake became aligned with the minor axis of the elliptical disk. This was ascribed to different growth rates in the plane of the major and minor axes. One may speculate whether or not the same phenomenon will occur in the wake behind a spheroid in crossflow as the spheroid does not possess any sharp edges from which the flow will separate.

2. Flow configuration and numerical method

In this study, we consider a geometrical configuration where the major axis of the prolate spheroid is aligned in the spanwise y direction and is six times larger than the minor axis. This yields an angle of incidence equal to 90° and an aspect ratio of 6:1. The governing equations are the time-dependent, incompressible Navier–Stokes equations for a viscous fluid. The Reynolds number is defined as $Re = U_o D/\nu$, where

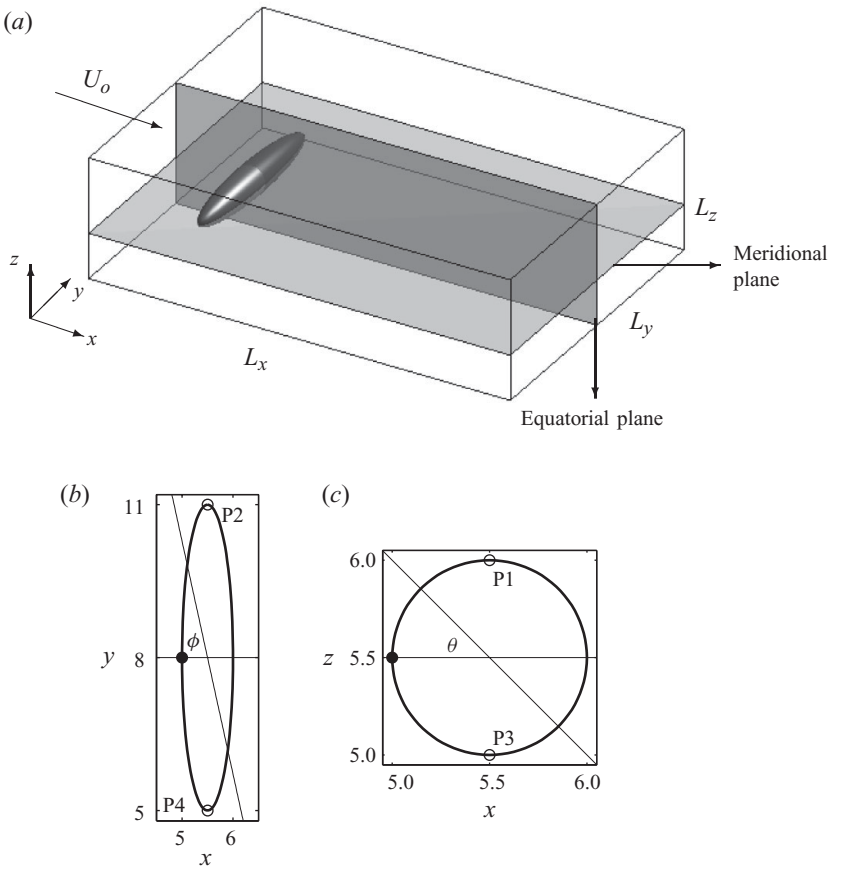

FIGURE 1. (*a*) Flow configuration and coordinate system (not to scale). (*b*, *c*) Cross-sectional views showing the azimuth (ϕ) angle in the meridional plane and the inclination (θ) angle in the equatorial plane. ●, Front stagnation point.

U_o is the uniform inflow velocity, D is the equatorial diameter of the spheroid and ν is the kinematic viscosity of the fluid.

The Navier–Stokes equations are solved using the well-documented direct numerical simulation (DNS) solver MGLET (Manhart 2004). MGLET is a finite-volume code in which the Navier–Stokes equations are discretized on a staggered Cartesian mesh with non-equidistant grid-spacing. The discretization of the advection and diffusion terms is second-order accurate. For time integration an explicit third-order Runge–Kutta scheme is used. The Poisson equation for the pressure is solved by the strongly implicit procedure (SIP) by Stone (1968).

The computational domain sketched in figure 1(*a*) has a streamwise length $L_x = 22D$, spanwise width $L_y = 16D$ and transverse height $L_z = 11D$. The centre of the spheroid is placed at $5.5D$, $8D$ and $5.5D$. This gives a minimum distance of $5D$ between the surface of the body and the borders of the computational domain. A total of $720 \times 656 \times 320$ points are used in x, y and z directions, respectively. A non-uniform mesh distribution is used in all the three non-homogeneous directions in order to adequately resolve the various scales in the boundary layers and the wake of the spheroid. The spheroid is embedded in a block with uniform grid spacings

x_m/D	1	3	5	7	9	11	13	15
$y/D = 6$	4.20	5.98	5.02	4.56	5.72	5.10	4.45	4.23
$y/D = 8$	7.72	6.30	6.75	7.49	6.19	10.4	9.77	9.57
$y/D = 10$	3.91	6.10	5.10	4.76	5.72	5.37	4.92	4.72

TABLE 1. Grid resolution $\Delta = \max(\Delta x, \Delta y, \Delta z)/\eta$ in the meridional plane at various streamwise positions measured from the major axis of the spheroid, i.e. $x_m = x - 5.5D$.

$\Delta x = 0.015D$, $\Delta y = 0.012D$ and $\Delta z = 0.008D$. A free-slip condition is imposed on the sides of the computational domain. At the inlet, a uniform flow with velocity U_o is prescribed and at the outlet a Neumann boundary condition is imposed for the velocities and the pressure is set to zero. A direct-forcing immersed boundary method (IBM) is used to interpolate the no-slip boundary conditions on the spheroid surface to the Cartesian mesh on which the computation is performed. For the interpolations, a least squares high-order method is employed. The detailed derivation, validation and implementation of the IBM technique in MGLET can be found in Peller *et al.* (2006). The time step is kept constant and equal to $0.001D/U_o$. The simulation utilizes 384 processors on an IBM P575+ parallel computer.

Throughout the present context, the following concepts will be used. The local Reynolds number, $Re_d = U_o d/\nu$, is based on the local diameter d along the spheroid's major axis. The (x, y) and (x, z) planes of symmetry of the spheroid will be referred to as the meridional and equatorial planes as shown in figure 1(a). The azimuth (ϕ) and inclination (θ) angles are measured from the front stagnation point in the meridional and equatorial planes, respectively (see figure 1b, c). Finally, the poles are defined as the extremities of the spheroid in the meridional plane.

In order to verify that the current simulation is an adequately resolved direct numerical simulation, the Kolmogorov length scale η is estimated as $(\nu^3/\varepsilon)^{1/4}$, where the energy dissipation rate $\varepsilon = \nu\overline{(\partial u_i/\partial x_k)^2}$ is evaluated from the simulated flow field. The local grid size Δ relative to the Kolmogorov length scale is presented in table 1 at different streamwise positions in the meridional plane. Provided that $\Delta \lesssim 5\eta$, all essential scales of the turbulence are resolved. The data in table 1 show that the adopted grid spacing is sufficiently fine to resolve almost all scales in the wake.

3. Results and discussion

3.1. *Shear-layer instabilities*

In order to study the temporal and spatial characteristics of the separating shear layer, time traces of the local skin-friction coefficient are depicted in figure 2 at four different locations on the spheroid's surface: $\theta = \pm 90^\circ$ in the equatorial plane and $\phi = \pm 90^\circ$ in the meridional plane, i.e. points P1, P2, P3 and P4 in figure 1(b, c). Here, the skin-friction coefficient is defined as $C_f = 2\tau_w/\rho U_o^2$, and τ_w is taken as the x-component of the wall shear stress vector, i.e. as $\tau_{xy} = \mu(\partial u/\partial y + \partial v/\partial x)$ at the poles P2 and P4, and as $\tau_{xz} = \mu(\partial u/\partial z + \partial w/\partial x)$ in the equatorial locations P1 and P3. Vigorous fluctuation levels are found to occur simultaneously in the shear layers emanating near the poles ($\phi = \pm 90^\circ$) whereas in the equatorial plane, the time traces exhibit more moderate fluctuations superimposed on a slowly varying signal. The time traces of the skin friction at the poles seem to fluctuate about an almost zero time-mean value. It is noteworthy that the major contribution to τ_{xy} comes from $\partial v/\partial x$, whereas $\partial u/\partial y$ varies irregularly about a small negative mean value at P2

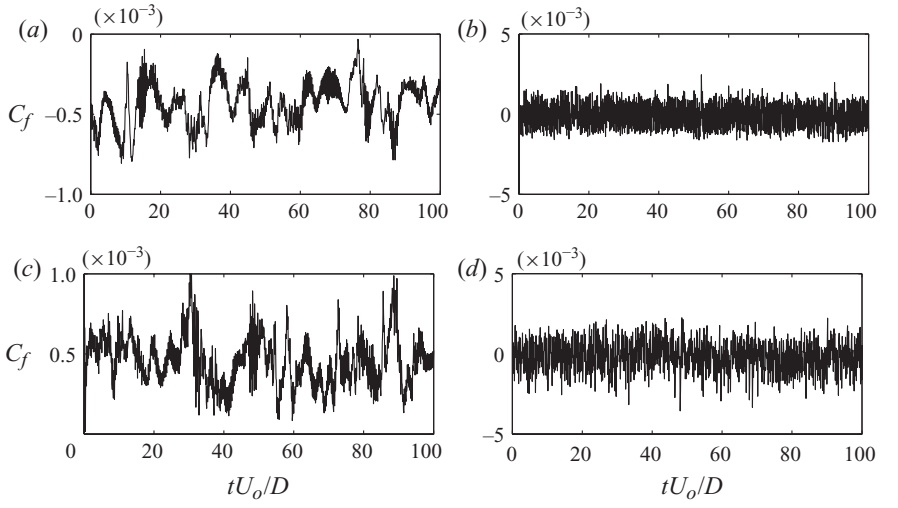

FIGURE 2. Time traces of the local skin-friction coefficient. (*a*) $\theta = 90°$, P1. (*b*) $\phi = 90°$, P2. (*c*) $\theta = -90°$, P3. (*d*) $\phi = -90°$, P4.

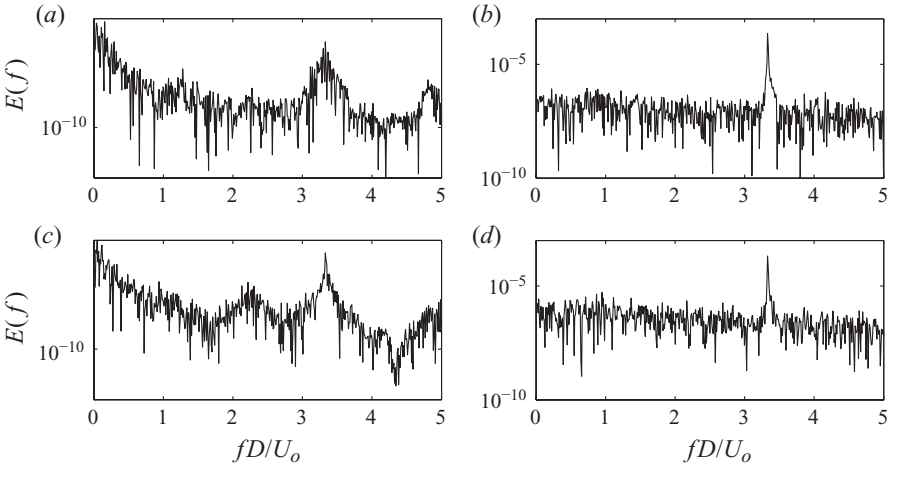

FIGURE 3. Power spectra of the local skin-friction coefficient. (*a*) $\theta = 90°$, P1. (*b*) $\phi = 90°$, P2. (*c*) $\theta = -90°$, P3. (*d*) $\phi = -90°$, P4. Notice the logarithmic scale along the vertical axis.

which thus implies that the mean flow separates only marginally upstream of the pole. The presence of a high-frequency mode at all four points indicates that the shear-layer instability occurs globally along the circumference of the spheroid in the (y, z) plane of symmetry. Such global high fluctuation levels were also observed by Yun *et al.* (2006) in the shear layer of uniform flow past a sphere at the same Reynolds number. In that case, Yun *et al.* (2006) took time traces of the radial velocity in the vortex ring at a streamwise location of D from the sphere centre.

The complexity in the skin-friction signals provides an impression of the chaotic nature of the flow pattern at this fairly high Reynolds number and is more evident in the accompanying frequency spectra presented in figure 3. In addition to a main frequency due to vortex shedding, which occurs at a Strouhal number $St \approx 0.156$ for points P1 and P3, the power spectra in figure 3(*a*, *c*) also contain an additional

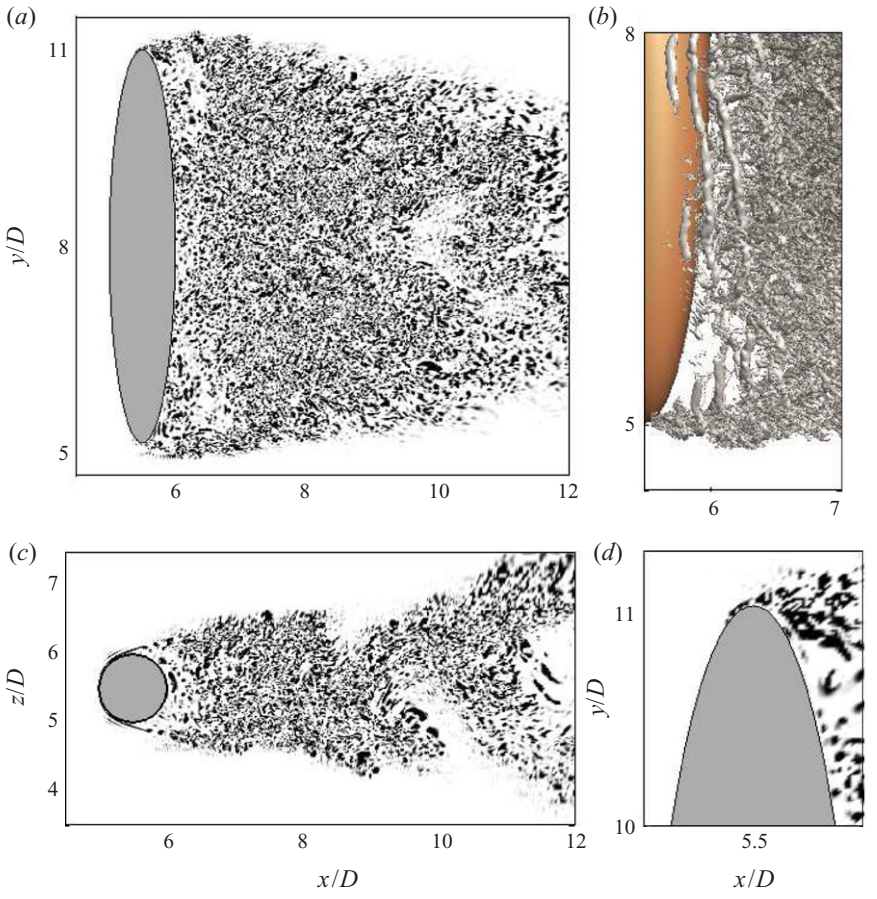

FIGURE 4. (Colour online) Instantaneous λ_2 values. (*a*) Meridional plane; (*b*) top three-dimensional view; (*c*) equatorial plane; (*d*) zoomed view of (*a*).

high-frequency component in the range $3.2 \leqslant fD/U_o \leqslant 3.4$. Such high frequencies are associated with the Kelvin–Helmholtz instability in the shear layers and were previously observed in the range $1.9 \leqslant St \leqslant 2.4$ by Constantinescu & Squires (2004) in their numerical investigation of uniform flow past a sphere at the subcritical Reynolds number 10 000. By considering the polar points P2 and P4, on the other hand, the power spectra show no evidence of a low-frequency component corresponding to the vortex-shedding mechanism. In fact, the distinct peaks occur at a single dominant frequency of $St = 3.33$, which is attributed to the shear-layer instability.

While figures 2 and 3 give a quantitative impression of the shear-layer instabilities, the separation of the boundary layer from the spheroid surface and the formation of Kelvin–Helmholtz vortices can be visualized by means of isocontours of λ_2 which are extracted following the method proposed by Jeong & Hussain (1995). Within the meridional plane and in the vicinity of the poles, figure 4(*a*) indicates a boundary layer separation where small-scale vortices are entrained into the wake. This behaviour is considerably different from that observed in the equatorial plane in figure 4(*c*). In this case, the separating shear layer remains laminar for a while and the Kelvin–Helmholtz instability occurs at an early stage that is upstream to the spheroid's rear stagnation point. Subsequently, the laminar shear layer eventually breaks up into small-scale

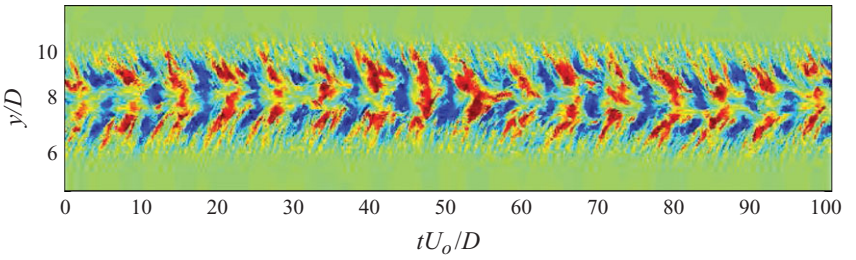

FIGURE 5. Time evolution of transverse velocity w/U_o at a position of $x_m = 3.5D$ from the major axis of the spheroid. Here, the colours vary from -0.7 (dark blue) to $+0.7$ (dark red) while light green represents 0.

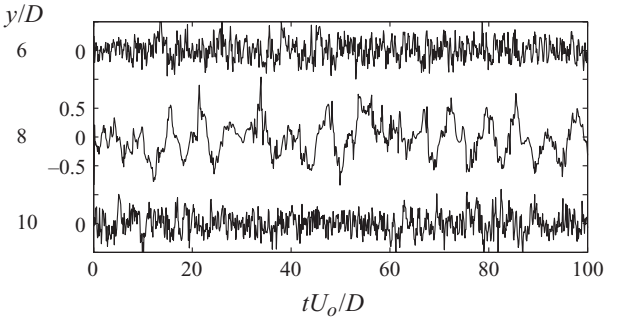

FIGURE 6. Time trace of transverse velocity w/U_o in the meridional plane at different spanwise locations taken along the sampling line located at $x_m = 3.5D$.

vortices and evolves into a turbulent state. Further observations that can be made from figure 4 will be discussed in § 3.3.

3.2. *Frequency analysis in the wake*

In order to investigate the shedding frequencies and instabilities in the wake, the time evolution of the velocity components u, v, w and pressure p has been evaluated within the meridional plane. The total simulated time was $100D/U_o$ which covers about 16 shedding cycles in the equatorial plane.

The time evolution of the transverse velocity w/U_o is shown in figure 5. The sampling is taken along a line parallel to the y-axis and located $3.5D$ downstream of the major axis of the spheroid. The herringbone pattern clearly indicates the oblique vortex shedding in the wake of the prolate spheroid. The alternating positive and negative values are associated with the large-scale vortex shedding and the resulting herringbone pattern is symmetric about the equatorial (x, z) plane. This large-scale mode seems to be mostly confined to a $4D$ wide band around the equatorial plane whereas a higher-frequency mode is apparent in the fringes of the wake. The time traces of w/U_o in figure 6 show beyond any doubt the differences in the signal near the poles and at the equator. The transverse velocity is more energetic downstream of the equator and associated primarily with the large-scale eddy shedding. Near the poles, on the other hand, the transverse motion is dominated by a high-frequency mode and the low-frequency vortex shedding is not discernible.

To further explore this phenomenon, frequency spectra were obtained by means of a Fourier transformation of time series like those in figure 6. The frequency f of the most energetic mode was obtained at all spanwise locations and the resulting local

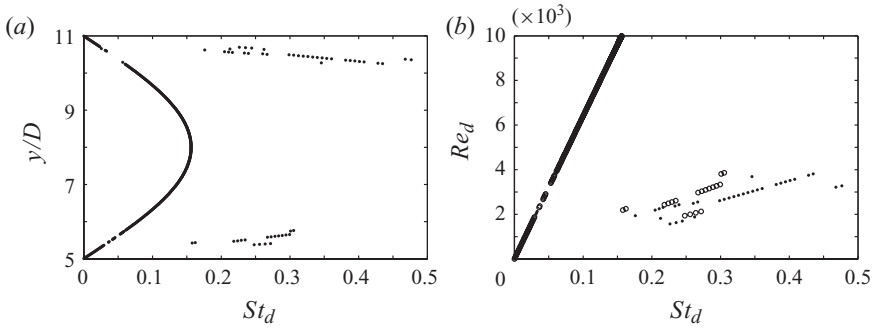

FIGURE 7. (*a*) Local Strouhal number St_d variation along a line parallel with the spheroid's major axis at $x_m = 3.5D$. (*b*) Local Strouhal number as a function of the local Reynolds number Re_d; ○, $5 < y/D < 8$; ●, $8 < y/D < 11$.

Strouhal number St_d defined as fd/U_o is shown in figure 7. It is readily observed that St_d increases from the poles towards equator where the maximum value 0.156 is reached. This is exactly the same Strouhal number value as that associated with the time variation of the skin-friction coefficient in the equatorial points P1 and P3 shown in figure 2(*a*, *c*).

However, in the vicinity of the poles, the flow is dominated by more high-frequency modes which give rise to local Strouhal numbers in the range from 0.15 to 0.50. These high-frequency modes are associated with the polar regions and their dominance over the shedding mode is confined to a distance $1D$ away from the pole. The high-frequency mode can be attributed to the Kelvin–Helmholtz instabilities in the separated shear layer. Yun *et al.* (2006) observed a similar co-existence of a shear-layer instability and wake instabilities in the wake behind a sphere at $Re = 10\,000$. They examined the time trace of the radial velocity component about $5.2D$ from the sphere axis in a plane which contained large-scale vortical structures. The resulting spectra showed a frequency component which was ascribed to the shear-layer instability. However, that particular frequency was substantially less energetic than the vortex-shedding frequency and the low-energy content was ascribed to the quasi-random time variation of the wavy structures in the azimuthal direction. In the present wake, on the other hand, the high-frequency mode is even more energetic than the shedding mode in a certain area.

The data in figure 7(*a*) can be plotted against the local Reynolds number as in figure 7(*b*). The low-frequency data from the two halves of the spheroid are seen to collapse and a linear St_d–Re_d variation is obtained. This simply implies that the shedding frequency f is constant along the span of the spheroid. Thus, in spite of the varying cross-section along the span, the shedding frequency remains the same. It should be emphasized that the gaps in the straight line correspond to certain spanwise locations where the high-frequency mode is more energetic than the low-frequency shedding mode, for instance as demonstrated by the upper and lower time traces in figure 6. These high-frequency modes associated with the shear-layer instability were clearly distinguishable $3.5D$ downstream of the major axis in figures 5–7. These modes are gradually attenuated with downstream distance and a high-frequency component is no longer discernible $9D$ downstream and only the lower-frequency shedding mode prevails.

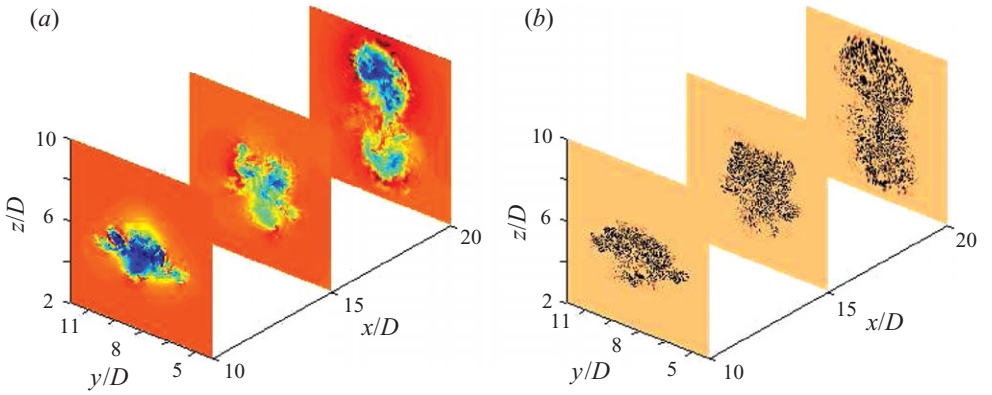

FIGURE 8. Cross-stream slices. (*a*) Instantaneous streamwise velocity u where the colours vary from 0.4 (dark blue) to 1.2 (dark red). (*b*) Instantaneous λ_2.

3.3. *Instantaneous vortical structures*

Instantaneous vorticity fields were visualized by means of λ_2 isocontours in figure 4. The perspective view in figure 4(*b*) gives a clear view of the shear-layer instability which occurs in the vortex sheet shortly after the shear layer separated from the surface of the spheroid. The presence of thin vortex filaments roughly aligned with the major axis can be observed. These filaments are fairly long but do not extend over the entire span. As they are convected downstream, they are distorted and eventually broken up by the vigorous motion in the near-wake.

The plots of λ_2 in the meridional and equatorial planes in figures 4(*a*) and 4(*c*), respectively, give the immediate impression that the wake contracts in the former and expands in the latter. At $x = 12D$, i.e. $6.5D$ downstream of the major axis, the width of the wake seems to be roughly the same in the y- and z-directions. The cross-stream slices depicted in figure 8 give another impression of this. It is particularly noteworthy that the axis of the wake has switched at $x = 20D$, in the sense that the major axis of the wake is now aligned with the minor axis of the spheroid. A similar axis switching was observed experimentally by Kuo & Baldwin (1967) and Kiya & Abe (1999) in the wake behind an elliptical disk. They reported that axis switching occurred at about $4D$ downstream of the disk, i.e. significantly closer to the bluff body than in this study.

4. Conclusions

The present investigation is apparently the first to explore a prolate spheroid in a crossflow, i.e. with the major axis perpendicular to the direction of the oncoming flow. This orientation breaks the axisymmetry of the laminar boundary layer at the frontal side of the body, the separated vortex sheet and the resulting wake flow. The Strouhal number 0.156 associated with the large-scale shedding was indeed significantly below that of the wake of a sphere at the same Reynolds number (Sakamoto & Haniu 1990; Constantinescu & Squires 2004). In spite of the spanwise variation of the diameter of the local cross-section, the vortex shedding occurred at one single frequency. This is in contrast to the cellular vortex shedding repeatedly observed behind tapered circular cylinders (Narasimhamurthy, Andersson & Pettersen 2009).

The flow around mid-span, i.e. in the equatorial plane in figure 4(*c*), resembled at first sight the flow past an infinitely long circular cylinder. However, the shedding

frequency of the large-scale vortices is substantially lower than that observed in the wake behind a circular cylinder. In the present case, fluid is sucked into the wake around the poles of the spheroid, as shown in figure 4(*d*). This inflow tends to widen the separated vortex sheet, increase the base pressure and reduce the shedding frequency.

The departure from axisymmetry excludes the presence of a helical vortex pattern as observed in the wake of a sphere by Sakamoto & Haniu (1990) and Yun *et al.* (2006). The shape of the near-wake reflected the elliptical shape of the meridional cross-section of the spheroid. Some $10D$ downstream, however, the major axis of the wake became aligned with the minor axis of the spheroid. Such axis switching has been reported earlier from experimental studies of the wake behind sharp-edged elliptical plates by Kuo & Baldwin (1967) and Kiya & Abe (1999). Since the same axis switching also occurred in the wake behind the prolate spheroid in this study, it can be concluded that this peculiar flow phenomenon depends only on the wake asymmetry and is otherwise independent of the actual bluff body.

A PhD research fellowship for the first author and computing time was provided by the Research Council of Norway.

REFERENCES

Constantinescu, G. S. & Squires, K. D. 2003 LES and DES investigations of turbulent flow over a sphere at $Re = 10\,000$. *Flow Turbul. Combust.* **70**, 267–298.

Constantinescu, G. & Squires, K. 2004 Numerical investigations of flow over a sphere in the subcritical and supercritical regimes. *Phys. Fluids* **16**, 1449–1466.

Han, T. & Patel, V. C. 1979 Flow separation on a spheroid at incidence. *J. Fluid Mech.* **92**, 643–657.

Jeong, J. & Hussain, F. 1995 On the identification of a vortex. *J. Fluid Mech.* **285**, 69–94.

Johnson, T. A. & Patel, V. C. 1999 Flow past a sphere up to a Reynolds number of 300. *J. Fluid Mech.* **378**, 19–70.

Kiya, M. & Abe, Y. 1999 Turbulent elliptic wakes. *J. Fluids Struct.* **13**, 1041–1067.

Kuo, Y. H. & Baldwin, L. V. 1967 The formation of elliptical wakes. *J. Fluid Mech.* **27**, 353–360.

Manhart, M. 2004 A zonal algorithm for DNS of turbulent boundary layers. *Comput. Fluids* **33**, 435–461.

Narasimhamurthy, V. D., Andersson, H. I. & Pettersen, B. 2009 Cellular vortex shedding behind a tapered circular cylinder. *Phys. Fluids* **21**, 044106–12.

Peller, N., Le Duc, A., Tremblay, F. & Manhart, M. 2006 High-order stable interpolations for immersed boundary methods. *Intl J. Numer. Methods Fluids* **52**, 1175–1193.

Sakamoto, H. & Haniu, H. 1990 A study on vortex shedding from spheres in a uniform flow. *J. Fluids Engng* **112**, 386–392.

Sheard, G. J., Thompson, M. C. & Hourigan, K. 2008 Flow normal to a short cylinder with hemispherical ends. *Phys. Fluids* **20**, 041701.

Stone, H. L. 1968 Iterative solution of implicit approximations of multidimensional partial differential equations. *SIAM J. Numer. Anal.* **5**, 530–558.

Wikström, N., Svennberg, U., Alin, N. & Fureby, C. 2004 Large eddy simulation of the flow around an inclined prolate spheroid. *J. Turbul.* **5**, 29.

Yun, G., Kim, D. & Choi, H. 2006 Vortical structures behind a sphere at subcritical Reynolds numbers. *Phys. Fluids* **18**, 015102–14.

Zdravkovich, M. M. 1997 *Flow Around Circular Cylinders.* Oxford University Press.